2 Quantitative Integrated Intensity Measurements by Pulsed Cavity Ringdown Spectroscopy: The ν_1 Band of Nitric Acid

2.1 Introduction

2.1.1 Spectroscopy of Nitric Acid

Nitric acid plays a critical role throughout the atmosphere as a reservoir for odd nitrogen species. In the troposphere, the formation of nitric acid from the reaction

$$OH + NO_2 \xrightarrow{M} HONO_2 \qquad \text{Reaction 2.1}$$

leads to radical chain termination and removal of nitrogen oxides through precipitation of nitric acid. In the stratosphere, the competition of nitric acid formation by reaction 2.1 and its destruction through reaction with OH or photolysis

$$OH + HONO_2 \longrightarrow H_2O + NO_3 \qquad \text{Reaction 2.2}$$

$$h\nu + HONO_2 \longrightarrow HO + NO_2 \qquad \text{Reaction 2.3}$$

largely determines the fraction of total nitrogen oxides that exist as the more reactive odd nitrogen species. As a result of its importance in the atmosphere nitric acid has been, and continues to be, the target of much research.

2.1.1.1 Infrared

The spectrum of nitric acid in the infrared has been studied by a number of groups to assist in atmospheric monitoring of nitric acid concentrations. The reported integrated intensities of the strongest band, the ν_1 O-H stretch, differ from each other by greater than 30% [22-24] leading to significant uncertainty in atmospheric HNO_3 measurements.

The ν_1 band has also been used in the studies of reaction 2.1 described in detail in chapters three and four. Reaction 2.1 has two possible products:

$$OH + NO_2 \xrightarrow{M} HONO_2 \qquad \text{Reaction 2.1a}$$

$$OH + NO_2 \xrightarrow{M} HOONO \qquad \text{Reaction 2.1b}$$

The yield of reaction 2.1b is pressure dependent and has important implications for our understanding of nitrogen oxides in the atmosphere. We measured this yield spectroscopically by measuring the ν_1 bands of HOONO and $HONO_2$ produced in reaction 2.1 with cavity-ringdown spectroscopy (CRDS). The high sensitivity of CRDS was critical to detecting and quantifying the low concentrations of the minor HOONO product. As described in the next section, however, the use of CRDS to measure the much higher concentrations resulted in systematic errors in retrieved nitric acid absorbances.

To understand and quantify these errors, we have measured the integrated absorbance of the nitric acid with IR-CRDS while simultaneously measuring the nitric acid concentration by direct absorption in the ultraviolet. The observed integrated cross section derived from our CRDS spectra was observed to vary as a function of pressure and nitric acid concentration. By extrapolating to conditions under which we expect no systematic error from CRDS, we make a new measurement of the nitric acid ν_1 integrated intensity.

2.1.1.2 Ultraviolet

The UV spectrum from 195 to 350 nm has been carefully studied, as photodissociation in this spectral region is the predominant loss process for nitric acid in

the stratosphere [25-31]. In addition to the large number of cross-section measurements at these wavelengths, the data sets are in very good agreement.

Due to absorption by molecular oxygen, the nitric acid cross section at wavelengths shorter than 195 nm is not relevant to the atmosphere and has not been as extensively studied [25, 32, 33]. However, the large value of the cross section at 184.9 nm (σ_{185}) and convenient Hg-lamp emission line at this wavelength provide a useful analytical tool for monitoring nitric acid concentrations. Absorption at 184.9 nm has been used previously in laboratory experiments of nitric acid, primarily for measurements of the rate constant for reaction 2.1 [32, 33].

We use the large cross section at 184.9 nm to measure the low nitric acid concentrations needed in our IR integrated intensity measurements. Due to the critical nature of σ_{185} to our IR CRDS experiments and the sparsity of reported values, we have re-measured σ_{185}.

2.1.2 Cavity Ringdown Spectroscopy

CRDS is an increasingly popular method for making measurements of very weak absorption spectra. A general description of the CRDS can be found in Chapter 1. Pulsed lasers with low resolution (0.1 to 1.0 cm^{-1} FWHM) are commonly used due to their wide tunability and ease of CRDS implementation, and the discussion here will be limited to pulsed systems. In an ideal CRDS experiment, subsequent to injection of a pulse of radiation to the optical cavity, the intensity of radiation in the cavity decays exponentially in time according to

$$I(t) = I_0 \exp\left[-\frac{tc}{L_{cav}}(A + (1-R)) \right], \qquad \text{Equation 2.1}$$

where t is time, c is the speed of light, L_{cav} is the length of the cavity, R is the reflectivity of the ringdown mirrors, and A is the absorbance by species X at concentration [X] molecules×cm^{-3} occupying length l_{abs} in the cavity. By fitting the observed decay to an exponential, the 1/e decay lifetime, τ, is obtained,

$$\tau = \frac{L_{cav}}{c}\left(\frac{1}{(1-R)+A} \right). \qquad \text{Equation 2.2}$$

The absorbance can then calculated by subtracting the background decay rate,

$$\frac{1}{\tau} - \frac{1}{\tau_0} = \frac{c}{L_{cav}} A, \qquad \text{Equation 2.3}$$

where τ_0 is ringdown time measured in the absence of the absorber. Generally, in a pulsed CRDS apparatus, τ_0 varies smoothly as the laser frequency is scanned with no influence from transverse modes of the cavity, as the short coherence length of the laser prevents the buildup of cavity mode structure in the ringdown cavity [13, 16].

The sensitivity and tunability of CRDS has been exploited by our group to simultaneously measure the infrared absorption of the ν_1 (OH stretch) bands of HOONO and $HONO_2$ formed in reaction 2.1 (chapters 3 and 4). While the high sensitivity of CRDS was necessary for detection and quantification of HOONO, the use of a low-resolution CRDS to make quantitative measurements introduces potential errors, particularly for the strongly absorbing, highly structured spectrum of nitric acid. With the broad frequency envelope of pulsed lasers (Γ_L = 0.1 – 1.0 cm^{-1} FWHM), the absorbance may vary within the frequency envelope of the laser. In this case, eq 2.1 no

longer describes the time profile of the cavity radiation, and the ringdown signal does not decay as a single exponential. For a frequency-dependent absorption, $A(\tilde{\nu})$, the observed ringdown is actually the combination of many different exponential decays described by

$$I(t,\tilde{\nu}_L) = I_0 \int_0^{\infty} L(\tilde{\nu}-\tilde{\nu}_L) \exp\left[\frac{tc}{l}\left[A(\tilde{\nu})+(1-R)\right]\right] d\tilde{\nu}, \qquad \text{Equation 2.4}$$

where $L(\tilde{\nu}-\tilde{\nu}_L)$ is a normalized function representing the laser profile centered at $\tilde{\nu}_L$. Attempts to fit an observed multi-exponential decay to a single decay lifetime τ lead to erroneous absorption results.

This is shown graphically for the simple case of a broad laser pulse interacting with a single sharp absorption feature in Figure 2.1. This specific case was thoroughly studied in the early days of CRDS to investigate the impact of fitting errors on retrieved CRDS spectra [14, 15, 18, 34]. Zalicki and Zare found that deviations occur when the laser linewidth Γ_{L} meets the condition $\Gamma_{\mathrm{L}} > \Gamma_{\mathrm{Abs}}/400$. Errors include incorrect line shapes and peak heights, incorrect integrated absorbance, and a dependence of the apparent absorption cross section on the size of the fitting window. At very low absorbance, while the line shape of a single feature is still not correctly determined, the absorbance is recovered "to within 10%" [18]. Zalicki and Zare propose that in order to obtain accurate absorbance measurements with low resolution lasers, the criterion $A < 0.1(1\text{-}R)$ must be met.

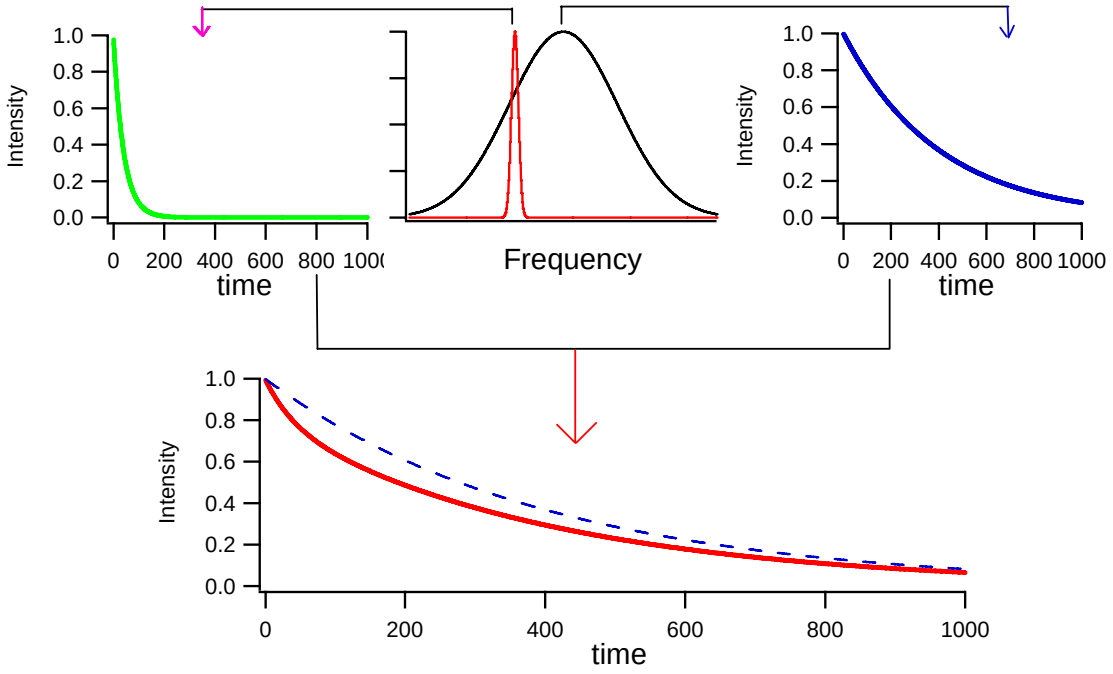

Figure 2.1. Representative ringdown decays for the case of a broad laser profile (black, top) probing a single narrow absorption feature (red, top). Frequencies corresponding to absorption will have fast decays (green), others will have slow decays (blue) identical to the empty cell. The observed decay is multi-exponential (red, bottom). The single-exponential empty-cell decay is shown as a dashed line for comparison.

While previous studies focused on the investigation of a single spectral line, there are no quantitative studies on a typical spectroscopy experiment of a small polyatomic molecule in which a low resolution laser scans a congested rovibrational spectrum. In this case, many lines that would be resolvable at high resolution are contained within the spectral bandwidth of the probe. It is not known how well CRDS measures the rotational envelope of congested spectra when using conventional nanosecond pulsed lasers with resolutions of 0.1 – 1.0 cm^{-1}. Figure 2.2 shows a high resolution FTIR spectrum of the ν_1 OH stretch of nitric acid [35].

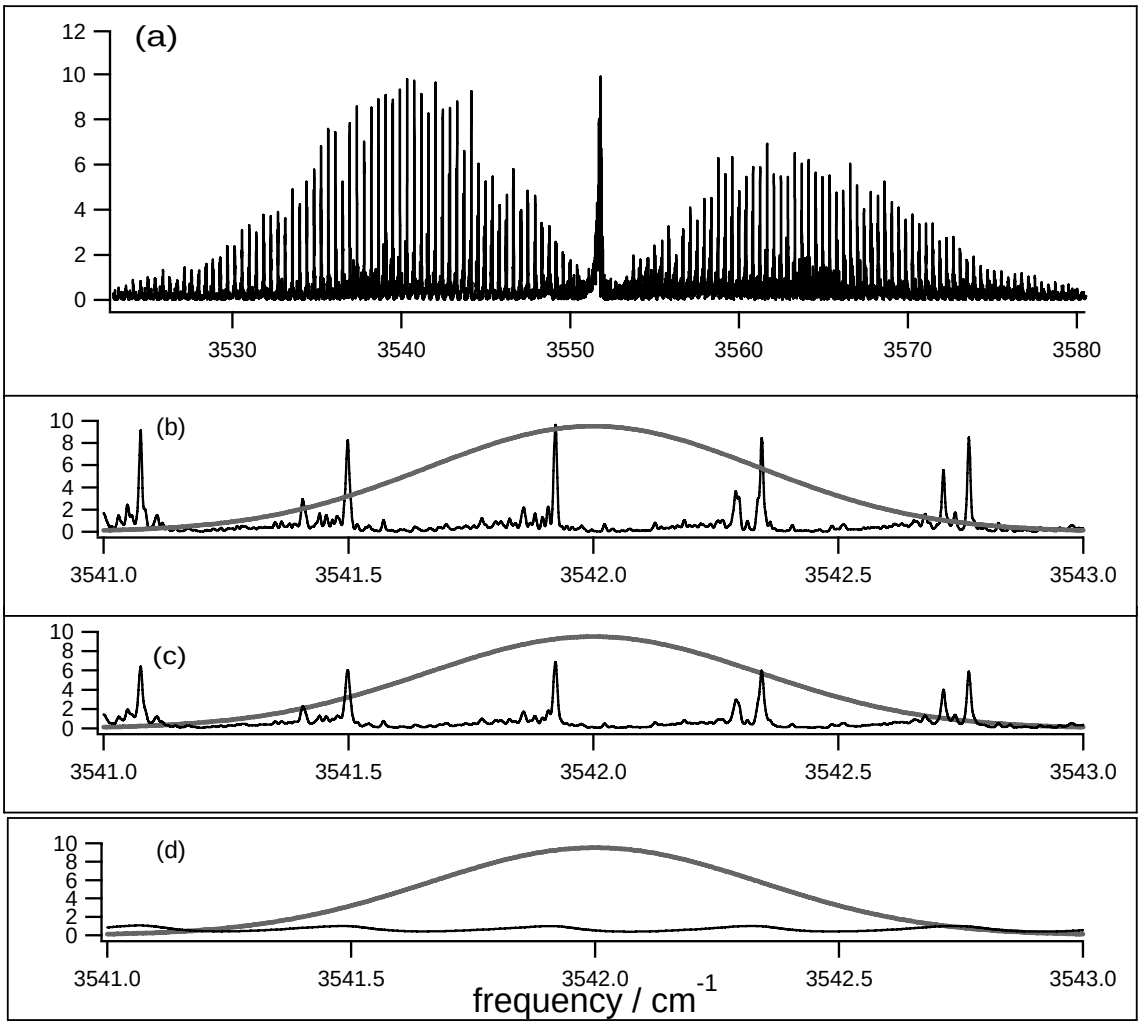

Figure 2.2. High resolution FTIR spectrum of the ν_1 band of nitric acid (panel a) in arbitrary units. (b)-(d) show a subset of the FTIR data (thin black line) with an approximation of our laser profile (thick grey line): (b) is the Doppler-limited spectrum, (c) is Lorentzian broadened to 0.0033 cm^{-1} FWHM (20 torr), (d) is Lorentzian broadened to 0.125 cm^{-1} FWHM (760 torr).

This is a congested band consisting of a small number of very sharp and intense features superimposed over a background of many weak, partially resolved lines. Panel (b) of Figure 2.2 compares a small portion of the FTIR spectrum with an assumed Gaussian laser profile (Γ_L = 1.0 cm^{-1}) superimposed in grey. For such a broad laser

width, the observed decay at each laser frequency, $\tilde{\nu}_L$, will be a multi-exponential; specifically the sum of a large number of exponentials each weighted by the intensity of the laser profile as described by eq 2.4. In general, the component decays that comprise the multi-exponential fall into two regimes: the very sharp features with large absorbance result in fast decay lifetimes and the broad background absorption results in much longer decay lifetimes.

Fits of a single exponential to these observed multi-exponential tend to give too much weight to the slow-decay component. This leads to measured CRDS absorbances from eq 2.3 lower than the true absorbance. These errors will depend on frequency, pressure and concentration, as the various component decays vary. As a result, we expect CRDS measurements of the v_1 band to have significant variations in the v_1 band shape and integrated absorbance, $IA(v_1)$.

In certain limiting cases, we would expect the error in our CRDS spectra to be negligible. At very high pressures, pressure broadening of the sharp features produces a more homogeneous underlying spectrum. As a result, fluctuations in $A(\tilde{\nu})$ over the laser profile are small, the decay is nearly a single exponential, and the observed integrated intensity should be accurate. At low concentrations, all components of the absorption contribute decays with long decay lifetimes. In this case, Zalicki and Zare's $A < 0.1\times(1\text{-}R)$ criterion is met for all components of the spectrum and again the integrated intensity should be accurate.

When not in the high-pressure or low-concentration limit, however, the observed CRDS spectrum will underrepresent the true molecular absorption, as the sharp features will contribute decays that are too fast to be captured by the single exponential fit. The

measured lifetime, τ, will therefore be dominated by the broad background absorption. CRDS errors should be the most dramatic at the peaks of the *P*, *Q* and *R* branches where the sharp features are the most intense. As a result we expect the nitric acid v_1 band shape and $IA(v_1)$ observed with CRDS to be both pressure and concentration dependent. The main goal of these experiments was to quantify these dependencies over a range of pressures and absorbances, paying particular attention to the conditions similar to those found in the relative kinetics measurements of reaction 2.1 (Chapters 3 and 4). To this end, three experiments were conducted: (1) experimental CRDS measurements of the nitric acid v_1 band shape and $IA(v_1)$ as a function of pressure and [HNO3], (2) CRDS simulations to reproduce the experimental v_1 band shape and $IA(v_1)$ data, and (3) CRDS measurements of $IA(v_1)$/ $IA(2v_2)$ as a function of pressure. From these experiments, corrections for CRDS $IA(v_1)$ measurements are derived and integrated cross sections for the nitric acid v_1, $S(v_1)$, and $2v_2$, $S(2v_2)$, bands are reported.

2.2 Cross Section at 184.9 nm

2.2.1 Experiment

A schematic of the apparatus is shown in Figure 2.3 with the setup labeled (a). Nitric acid was introduced by flowing He through a temperature-controlled bubbler containing pure nitric acid. The nitric acid flow was diluted with N_2 before entering the first flow cell (Cell A), where the concentration was measured, then further diluted with N_2 before entering the second flow cell (Cell B), where the absorption at 184.9 nm was measured.

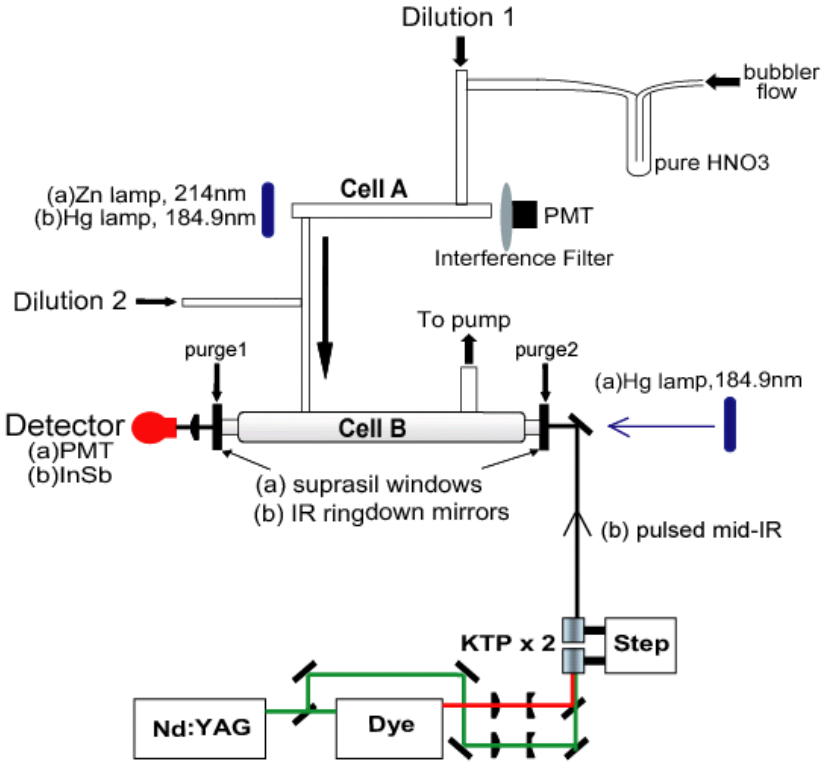

Figure 2.3. Schematic of the flow cell apparatus used for (a) measuring the nitric acid 184.9 nm UV cross section and (b) measuring the ν_1 and $2\nu_2$ integrated absorption by IR-CRDS.

2.2.1.1 UV Absorbance

The nitric acid concentration was measured in Cell A by UV absorption at 214 nm. Cell A was 30.2 cm long with an inside diameter of 1.0 cm and UV-grade quartz windows. 214 nm radiation was produced by a Zn lamp (UVP), collimated through a series of lenses and irises, passed through cell A and detected with a bialkali PMT equipped with a 214 nm interference filter. For each 184.9 nm absorption measurement, the concentration of nitric acid in Cell B, $[HNO_3]_{185}$, was calculated using eq 2.5.

$$[HNO_3]_{185} = \frac{-\ln\left(\frac{I_{214}}{I_{0,214}}\right)}{L_{214}\sigma_{214}}\left(\frac{P_{185}}{P_{214}}\right)\left(\frac{f_{214}}{f_{185}}\right), \qquad \text{Equation 2.5}$$

where $-\ln\left(\frac{I_{214}}{I_{0,214}}\right)$ is the Beer's Law absorption in Cell A, σ_{214} is the cross section at 214 nm ($\sigma_{214} = 4.33\times10^{-19}$ cm^2 molecule^{-1}) [36], L_{214} is the length of Cell A (L_{214}), and the last two factors are the ratios of flows and pressures in the two cells. Nitric acid concentrations in Cell A were typically on the order of 10^{16} molecules×cm^{-3}, leading to 214 nm absorbances of about 0.1. The total pressure in the system was kept at about 40 torr and P_{185}/P_{214} was typically between 0.9 and 1. The total flow in the system varied from 200 to 2000 sccm, with f_{214}/f_{185} ranging from 0.05 to 0.3, resulting in Cell B nitric acid concentrations of 4-50×10^{14} molecules×cm^{-3}.

Cell B had a total length of 47 cm, with suprasil windows mounted to either end. The sample was confined to the center of Cell B by purge flows of UHP Ar over the ends, as discussed below. 184.9 nm radiation was produced by a Hg Pen-Ray lamp (UVP), collimated through a series of lenses and irises, passed through cell B and detected with a bi-alkali PMT equipped with two 184.9 nm interference filters. Leakage of 254 nm light through the 185 nm interference filter was quantified each day by saturating the absorption at 185 nm with N_2O ($\sigma_{185} > 10^4\times\sigma_{254}$). The 254 nm intensity, on the order of 1% to 3% of the empty cell intensity, was subtracted from all intensity measurements. Leakage from the nearby Hg emission line at 195 nm was measured by absorption of CO_2 to be 9.5% of the of the empty cell intensity, and was also subtracted from all intensity measurements. The uncertainty of individual intensity measurements were 0.7% for 184.9 nm and 0.5% for 214 nm. Background UV readings were measured before and after each point. The background drifted slightly over the course of the data collection, so the average of the background readings surrounding each point was used.

2.2.1.2 Sample Path Length

The effective path length of sample in Cell B, l_s, was measured by flowing pure N_2O through the center of Cell B and measuring the absorbance at 214 nm as a function of purge flow. The UV apparatus was first tested by measuring the N_2O absorbance of the cell filled completely to a given pressure of pure N_2O. We measured a cross section of $\sigma_{214} = 3.48\times10^{-21}$ cm^2 molecule^{-1}, within 2% of the literature value [36], using $l_s = L_{tot}$ = 53 cm (Figure 2.4).

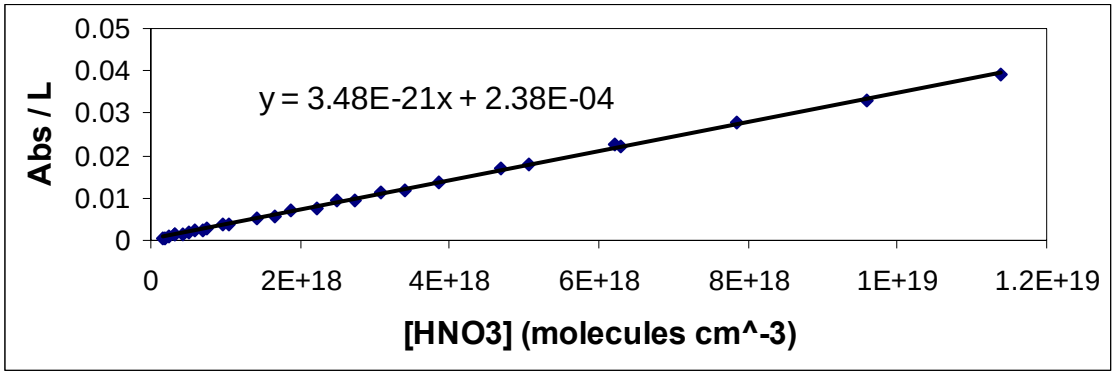

Figure 2.4. Static cell measurements of N_2O absorbance at 214 nm.

Figure 2.5 shows the variation in l_s with purge flow. When the purge flows were small l_s varied rapidly with purge, dropping to 23 cm at purge flows 3% of the total flow ($0.03F_{tot}$). The dependence of l_s upon purge at higher purge flows was much more gradual, with l_s = 17 cm at $0.13F_{tot}$. We found that l_s was also weakly dependent upon pressure. As a result of the dependence upon purge flow, an attempt was made conduct all subsequent experiments keeping the purge flow over each end at $0.07F_{tot}$ to keep $l_s \approx$ 19.5 cm. The dependence of l_s upon purge and pressure was parameterized and the specific flow conditions for each measurement were used to calculate l_s. Calculated l_s values are estimated to have a 2σ uncertainty of 3%.

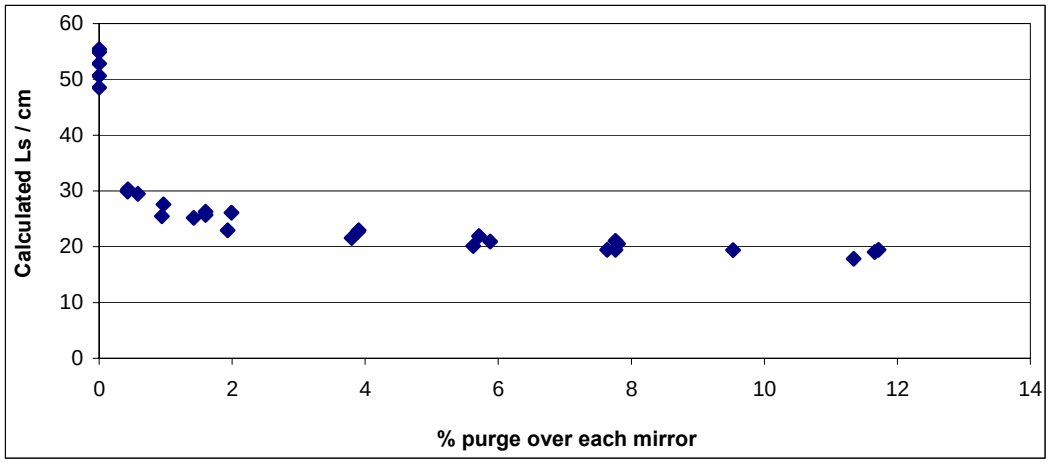

Figure 2.5. Variation in sample path length as a function of purge flow. *Ls* was calcuated using σ_{214} = 3.48×10^{-21} cm^2 $molecule^{-1}$

2.2.1.3 Gases

All flows were measured with Edwards or Omega mass flow transducers, calibrated volumetrically and were accurate to 0.5%. The pressure was measured from ports in the center of both cells using MKS Baratrons, calibrated with a JPL calibration system consisting of MKS 10 torr and 1000 torr calibration heads accurate to within 0.05% from a recent factory calibration. Corrections to our pressure readouts were generally less than 5% and corrected values should be accurate to 0.5% over the range of pressures used in this study. The pressures and flows remained constant for the duration of each data point.

Nitric acid was synthesized by adding concentrated H_2SO_4 to $NaNO_3$ under vacuum, collecting the nitric acid vapor in a liquid N_2 cold trap. When not being used the sample was stored in a liquid N_2 dewar. After storage, the sample would contain small quantities of the decomposition product NO_2. After bubbling for about 5 minutes, the NO_2 would completely evolve leaving pure nitric acid. This process was confirmed by

connecting our flow system to a Nicolet FTIR spectrometer and monitoring the NO_2 absorption in time. All tubing, valves, and joints between and including Cell A and Cell B were either glass or teflon to minimize surface decomposition.

2.2.2 Results

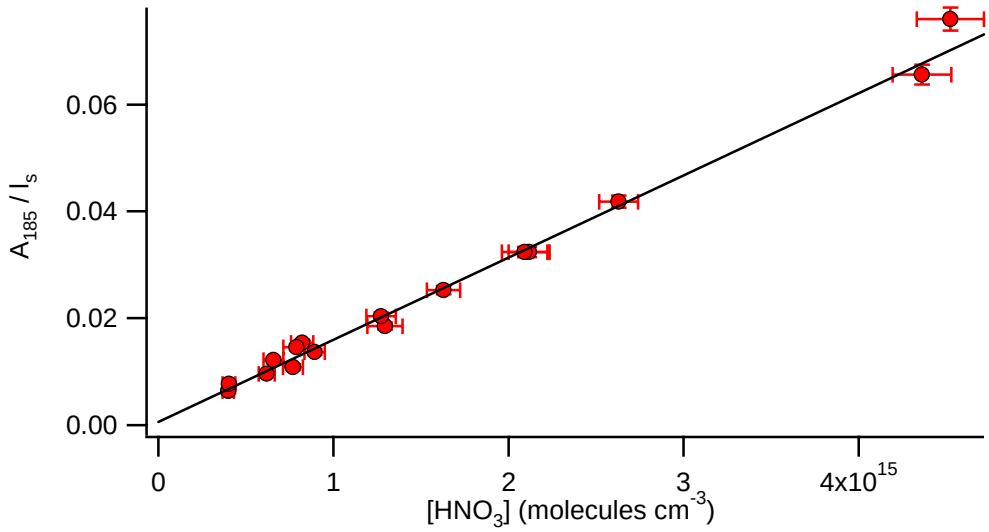

Figure 2.6. (A_{185} / l_s) as a function of nitric acid concentration. Nitric acid concentration is calculated from eq 2.5. The slope of the fit yields a 184.9 nm cross section of 1.55±09×10^{-17} cm^2×molecule^{-1}

The 184.9 nm Beer's Law absorbance A_{185} divided by l_s at room temperature is plotted as a function of nitric acid concentration in Figure 2.6. The error bars on each point represent propagated 2σ uncertainties. Uncertainties in the *y*-axis are dominated by the 0.7% uncertainty in I_{185}, which lead to 2%-6% uncertainties in A_{185}, and the 3% uncertainty in l_s. The uncertainty in l_s stems from the scatter in measurements of l_s (see Figure 2.5 above) and thus has been treated as a random uncertainty. Ucertainties in the *x*-axis are dominated by the 0.5% uncertainty in I_{214}, which leads to 5%-9% uncertainties in A_{214}. Other sources of uncertainty in [HNO_3], such as in the literature value of σ_{214}

and uncertainties in the pressure and flow measurements, are less than 1% and therefore contribute little to the overall uncertainty.

A weighted fit of the data yields $\sigma_{185} = 1.55 \pm 0.09(2\sigma) \times 10^{-17}$ cm^2 molecule^{-1}. The intercept of 0.0006 ± 0.0009 is of the same order as our uncertainty in an individual measurement of the absorbance, indicating no significant systematic error.

2.2.3 Discussion

Table 2.1 lists our value of $\sigma_{184.9}$ along with the most recently reported values in the literature [25, 32, 33]. The previous studies differ from each other and this study in many ways, making assessment of their relative merits difficult. The most significant difference stems from the nature of the gas handling in each experiment. This study uses a diluted flow of nitric acid, Connell continuously flows pure nitric acid through the cell, while Biaume and Wine et al. fill static cells. Using a constant flow of nitric acid as in this study and Connell reduces possible complications from decomposition of nitric acid to form NO_2. Wine et al. report a significant variation in their measured cross section depending on the how many fills they have done between extensive pumping on the cell. They attribute this variation to conditioning of their cell and this leads to their wide range of reported values. Biaume does not report any such effect. Wine and Connell use small cells (2.5 cm) and measure low pressures of nitric acid directly in the cell while Biaume, for wavelengths shorter than 200 nm, measures the pressure of nitric acid in a small volume and then expands it into a larger cell.

Table 2.1. HNO_3 184.9 nm cross section measured in this work compared to literature data. Reported uncertainties are 2σ. Wine et al. report only a range of observed values.

Study	year	static/flow	$[HNO_3]$ measurement	$\sigma_{184.9}$ / $cm^2 \times molecule^{-1}$
this work	2004	flow	214 nm UV absorption/dilution	$1.55 \pm 0.09 \times 10^{-17}$
Biaume [25]	1998	static	HNO_3 pressure/expansion	$1.63 \pm 0.05 \times 10^{-17}$
Connell / Howard [32]	1985	flow	HNO_3 pressure	$1.64 \pm 0.03 \times 10^{-17}$
Wine et al. [33]	1981	static	HNO_3 pressure	$1.45\text{-}1.70 \times 10^{-17}$

The procedure used in this experiment of measuring the nitric acid concentration with a well-known UV cross section is unique among the measurements of $\sigma_{184.9}$. Using a continuous and fairly rapid flow has several advantages, primarily a reduced potential influence of nitric acid decomposing or sticking to the walls of the cell. The main drawback of this technique is the increase in measurement uncertainties, such as the doubling of the number of intensity measurements and the uncertainty in l_s. Overall, our value for σ_{185} is about 5% lower and has slightly larger error bars than the most commonly used value of Biaume; The two measurements do agree within their uncertainties. The agreement between our value and the previous literature indicates that our flow-cell apparatus, where $[HNO_3]$ is determined by UV absorption, can yield accurate cross-section measurements. The IR experiments described below utilize our value for $\sigma_{185} = 1.55 \times 10^{-17}$ $cm^2 \times molecule^{-1}$.

2.3 IR Integrated Intensities

2.3.1 Experiments

A schematic of the apparatus is shown in Figure 2.3 with the setup labeled (b). The concentration of nitric acid carried in N_2 was measured by 184.9 nm absorption in Cell A. The details of Cell A and 184.9 nm absorption measurements are given above. The flow was then further diluted with N_2 before entering Cell B, where the IR-CRDS spectrum was taken. The concentration of nitric acid in Cell B was calculated using eq 2.6.

$$[HNO_3]_{IR} = \frac{-\ln\left(\frac{I_{185}}{I_{0,185}}\right)}{L_{185}\sigma_{185}}\left(\frac{P_{IR}}{P_{185}}\right)\left(\frac{f_{185}}{f_{IR}}\right), \qquad \text{Equation 2.6}$$

where $-\ln\left(\frac{I_{185}}{I_{0,185}}\right)$ is the Beer's Law absorption in Cell A, L_{185} = 20.2 cm is the length of Cell A, $\frac{P_{IR}}{P_{185}}$ and $\frac{f_{185}}{f_{IR}}$ are the ratio of flows and pressures in the two cells, and σ_{185} = 1.55×10^{-17} $cm^2\times molecule^{-1}$ (Section 2.2). Nitric acid concentrations in Cell A were in the range $2\text{-}14\times10^{14}$ $molecules\times cm^{-3}$, leading to 185 nm absorbances ranging from 0.1 to 0.7. The total pressure in the system varied from 18 to 760 torr. At higher pressures, P_{185}/P_{214} was typically very close to 1, whereas at low pressures and high dilution flows was as small as 0.6. The total flow in the system varied from 500 to 4000 sccm, with f_{214}/f_{185} ranging from 0.03 to 0.2, resulting in Cell B nitric acid concentrations of $(7\text{-}500)\times10^{12}$ $molecules\times cm^{-3}$. Cell B was the same as that described above, but with the suprasil windows replaced with ringdown mirrors (L_{cav} = 45 cm). As described above (Section 2.2.1.2), the sample path in Cell B, l_s, was calculated from the pressure and flows for

each experiment, with $l_s \approx 19$ cm. Gases, flowmeters, and pressure transducers were all the same as described in Section 2.2.1.3.

Infrared spectra were collected in Cell B using moderate resolution (1 cm^{-1}) IR-CRDS. Details of the laser system and CRDS apparatus are given in Chapter 1. For these experiments, typical background ringdown times were about 7 μs and about 5 lifetimes were collected and fit. Scanning of the OPA system, collection of the spectra, and the fitting of accumulated ringdown traces were controlled by a Labview PC program.

Scans investigating changes in our observed v_1 spectral shape were taken from 3490-3610 cm^{-1} at 0.2 cm^{-1} step size. Scans measuring $IA(v_1)$ as a function of pressure and [HNO_3], were taken in pairs: from 3480 to 3620 cm^{-1} at 4 cm^{-1} step size and from 3530 to 3570 cm^{-1} at 1 cm^{-1} step size. Scanning in this manner enabled us to capture the shape surrounding the Q-branch, while significantly reducing the time needed to scan over the entire v_1 band. The agreement of the 4 cm^{-1} and 1 cm^{-1} scans at all overlapping points assured us there was no drift in nitric acid concentration on the time scale of the scans (10 minutes). Scans measuring the relative integrated absorption of the v_1 and $2v_2$ bands were taken over the range 3330-3620 cm^{-1} at 1.5 cm^{-1} step size.

Background CRDS scans were taken before and after at most every 4 scans of the nitric acid peak. Background scans showed no sign of outgassing from residual nitric acid adsorbed to the walls. Additionally, each nitric acid scan extended 10 cm^{-1} beyond the nitric acid band on either side, serving as an inherent measure of the background τ_0 with each scan. The integrated absorbance was calculated from the measured ringdown

lifetimes with (τ) and without (τ_0) an absorber by integrating the standard ringdown equation (eq 2.3) for absorbance over the entire band profile.

$$IA(\nu_1) = \int_{3490\ \mathrm{cm}^{-1}}^{3610\ \mathrm{cm}^{-1}} \mathrm{Abs}(\tilde{\nu})\mathrm{d}\nu = \frac{L_{cav}}{c} \int_{3490\ \mathrm{cm}^{-1}}^{3610\ \mathrm{cm}^{-1}} \left(\frac{1}{\tau(\tilde{\nu})} - \frac{1}{\tau_0(\tilde{\nu})} \right) \mathrm{d}\tilde{\nu}\,.$$

$IA(2\nu_2)$ was calculated similarly, with the bounds of integration changed to 3350-3450 cm^{-1}.

2.3.2 Simulations

The IR-CRDS nitric acid spectrum was also investigated using a CRDS simulation program. The program convolved an assumed high resolution spectrum and laser profile (Figure 2.2) into multi-exponential CRDS decays. This was accomplished by first broadening the high-resolution spectrum with Lorentzians to the pressure of interest (γ = 0.125 $cm^{-1}\times atm^{-1}$ was used, discussed below). The pressure-broadened spectrum was then scaled to the desired absorbance and each point converted from absorbance units to a ringdown lifetime, τ. These τ were then added to an assumed background τ_0 (set to 7 μs as in the experiments), converted to exponential decays, and summed over a normalized Gaussian centered at $\tilde{\nu}_\mathrm{L}$, $L(\tilde{\nu} - \tilde{\nu}_L)$, representing the laser profile (Γ_L = 1.0 cm^{-1} was used, discussed below)

$$I(t, \tilde{\nu}_L) = I_0 \sum^{\text{all points}} L(\tilde{\nu}_i - \tilde{\nu}_L) \exp -\left[\tau(\tilde{\nu}_i) + \tau_0 \right] \qquad \text{Equation 2.7}$$

To expedite the simulations, the above sum was carried out only over points within $\tilde{\nu}_\mathrm{L} \pm \Gamma_\mathrm{L}$ (98% of laser profile intensity), rather than for all points. Tests using $\tilde{\nu}_\mathrm{L} \pm 1.5\Gamma_\mathrm{L}$ showed no change in simulation results. The decays generated by eq 2.7 were then fit

using the same nonlinear Levenberg-Marquardt algorithm used to fit our experimentally observed decays. The center frequency of the laser profile, $\tilde{\nu}_L$, was then scanned over the entire band profile. In this way, changes in the ν_1 band shape and $IA(\nu_1)$ were investigated as a function of pressure and [HNO_3] in the same manner as in the experiments described above.

In addition to the absorbance derived from our fits to these multi-exponentials, the true absorbance with no CRDS fitting error, $IA(\nu_1)_{Ture}$, was also obtained by summing the lifetimes over the laser profile prior to converting to exponential decays. In order to compare the simulation results to the experimental results, $IA(\nu_1)_{True}$ was converted to a nitric acid concentration using an assumed value for the integrated cross section $S(\nu_1)$ = 1.22×10^{-17} cm molecule^{-1} [22].

$IA(\nu_1)_{True}$ was also used to calculate the magnitude of the CRDS error, E_{CRDS}, from the simulations where

$$E_{CRDS} = \frac{IA(\nu_1)_{CRDS}}{IA(\nu_1)_{True}},$$

Due to the limited range of the high-resolution FTIR spectrum used for the simulations, the simulated CRDS and true absorbance spectra are limited to the range 3525-3579 cm^{-1}. It was assumed that the missing absorbance in the far wings was well approximated by the experimentally observed spectra. Any error in this assumption was likely small and had a negligible impact on simulated $IA(\nu_1)_{CRDS}$ since the far wings contribute <2% to the total integrated absorbance.

Calculated E_{CRDS} were then used to correct the low-[HNO_3] experimental $IA(\nu_1)$ to eliminate the impact of CRDS fitting errors prior to deriving $S(\nu_1)$ from the

experimental data. Due to the low concentrations involved, variations in E_{CRDS} for these data were small. As a result, our derived integrated cross section was insensitive to the value of $S(\nu_1)$ used to calculate [HNO_3] for the simulation data, varying by less than 1% over the range $S(\nu_1) = (1.0–1.5)\times10^{-17}$ cm molecule^{-1}.

Assumed values for the laser linewidth, Γ_L, and the pressure-broadening coefficient, γ, were critical inputs to the CRDS simulations. As a result, both Γ_L and γ were systematically varied to determine the sensitivity of simulated outputs to these parameters and confirm the validity of our assumed values. Since previous measurements using our OPA system had indicated $\Gamma_L \approx 1.0$ cm^{-1}, the range $\Gamma_L = 0.5$-2.0 cm^{-1} was used to generate simulated spectra. Simulated $IA(\nu_1)$ showed a negligible dependence upon Γ_L. The change was largest at the highest concentrations, but even at 2800×10^{-12} molecules×cm^{-3}, doubling Γ_L led to only a 0.7% decrease in $IA(\nu_1)$. Similarly, halving Γ_L led to only a 1.5% increase in $IA(\nu_1)$. Changes in the simulated ν_1 band shape with Γ_L, particularly in the region around the Q branch at low pressures, were more pronounced. Only Gaussian line shaes in the range Γ_L = 0.8-1.2 cm^{-1} produced reasonable matches to the experimentally observed spectra, with the best fit coming with $\Gamma_L = 1.0$ cm^{-1}.

Literature measurements of pressure broadening coefficients for pure rotational transitions in nitric acid (γ = 0.11 cm^{-1}×atm^{-1} in N_2 [37]) and ν_1 rovibrational transitions of OH (γ = 0.146 cm^{-1}×atm^{-1} in N_2 [38]) led to testing the range γ = 0.09-1.70 cm^{-1}×atm^{-1} in our simulations. While any values of γ > 0.10 cm^{-1}×atm^{-1} were able to match the observed spectral shape at 1 atm, only the very small range of γ = 0.120-0.130 cm^{-1}×atm^{-1} were successfully able to match both the high- and low-pressure experimental spectra.

The quantitative impact of changing γ over this range was largest at the lowest pressures studied and less than 2% under all conditions.

2.3.3 Results

Four scans of the ν_1 band of nitric acid taken at 0.2 cm^{-1} step size for various concentrations and pressures are shown in Figure 2.7. Both experimental and simulated spectra are shown for four conditions: 750 torr at 6.0×10^{13} and 1.0×10^{15} molecules$\times cm^{-3}$ and 20 torr at 4.2×10^{13} and 1.0×10^{15} molecules$\times cm^{-3}$. For comparison, the simulated true absorbance with no CRDS fitting error is also shown. In the bottom panel the experimental scans have been normalized to 1.0×10^{14} molecules$\times cm^{-3}$ in order to emphasize the change in spectral shape. The experimental and simulated spectra agree quite well in both shape and intensity under all conditions. As expected, the absorbance loss due to CRDS fitting errors is much more dramatic in the 20 torr spectra, with considerable loss in the most intense regions of the spectrum even at the lower concentration. While the 750 torr exhibits much smaller CRDS effects, changes in the spectral shape from the data to the true absorbance and between the two concentrations are still apparent in the heights of the Q-branch.

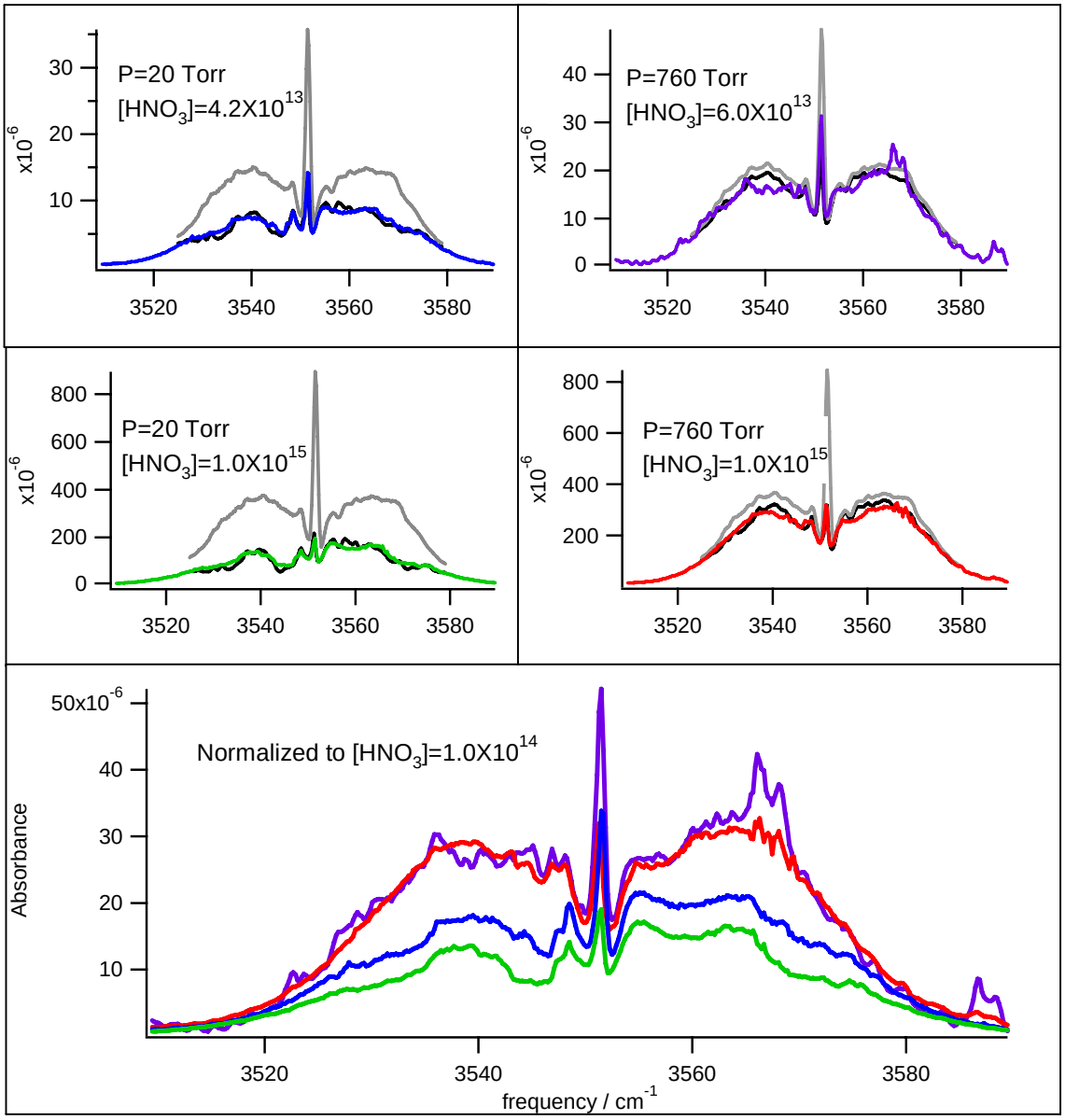

Figure 2.7. Experimental and simulated IR-CRDS spectra of the ν_1 OH stretch of nitric acid. Colored spectra are experimental data, CRDS simulations are shown in black, and the grey spectra represent the expected spectral shape with no CRDS error. All concentrations in molecules×cm^{-3}. The bottom panel shows the four experimental spectra from the upper panels normalized to 1×10^{14} molecules×cm^{-3}.

Figure 2.8 shows collected ringdown traces at two frequencies from the low pressure, high concentration spectrum shown in Figure 2.7 along with the fits and residuals for those traces.

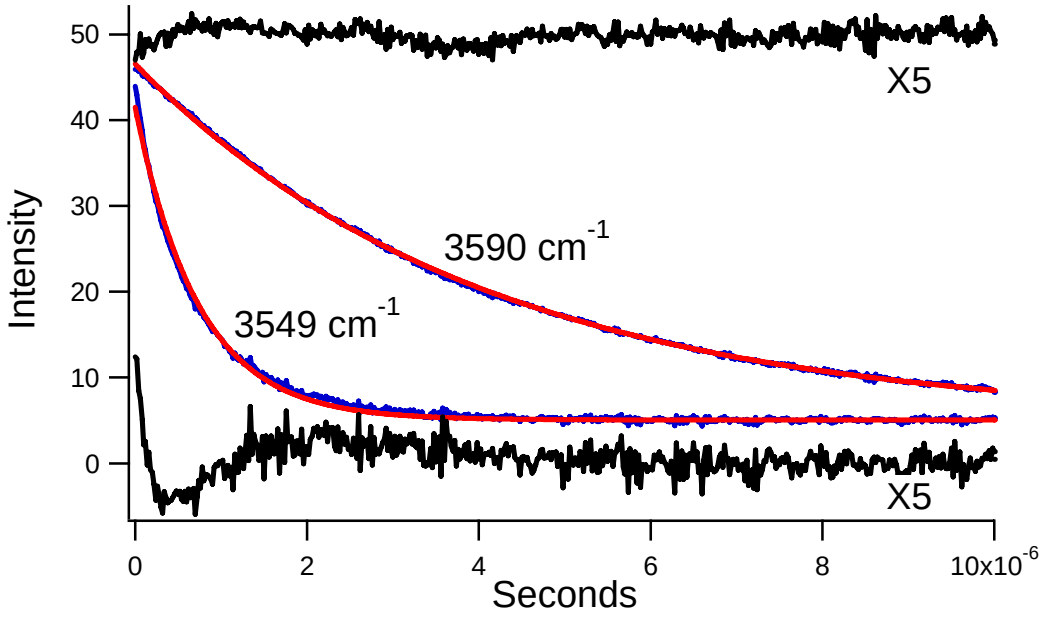

Figure 2.8. Two measured ringdowns (blue) along with the Levenberg-Marquardt fits (red) and residuals. The residuals have been multiplied by 5 for clarity. The residual for the 3549 cm^{-1} trace is shown at the bottom, while the residual for the 3590 cm^{-1} trace has been offset by 50.

The mechanism for the dramatic reduction in absorbance in the intense regions of the low pressure CRDS spectra is evidenced by the poor fit to the 3549 cm^{-1} trace. The observed multi-exponential decay is poorly fit by a single exponential, particularly at early times, when the contribution of the sharp, intense features is rapidly changing. As expected, the fit to the trace taken at 3590 cm^{-1} is much better, as the spectrum is more homogeneous and all absorbances are much smaller in this region. Residuals such as that shown in the bottom of Figure 2.8 are found, to varying degrees, for all regions of nitric acid spectra where a reduction in CRDS spectral intensity is observed.

$IA(\nu_1)/l_s$ data taken at 20 and 630 torr are plotted as a function of nitric acid concentration in Figure 2.9. Again, both experimental and simulated CRDS data are shown along with the simulated true $IA(\nu_1)/l_s$ in the absence of CRDS error. The

uncertainties in individual experimental $IA(\nu_1)/l_s$, on the order of the scatter in the data, have been omitted for clarity.

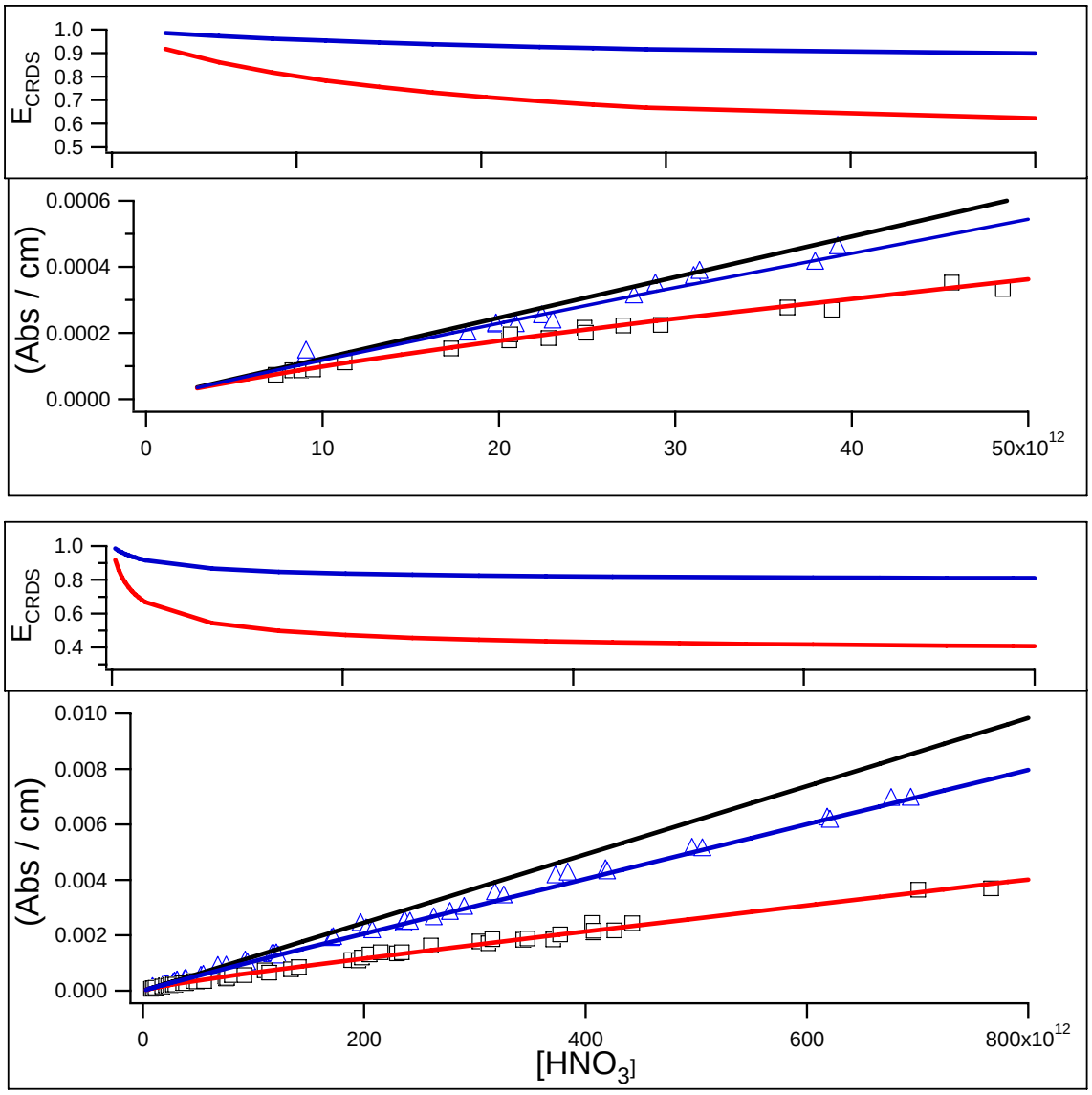

Figure 2.9. ($IA(\nu_1)/l_s$) as a function of nitric acid concentration. Triangles are data taken at 630 torr, squares are data taken at 20 torr. The blue line is the CRDS simulation at 630 torr, the red line is the CRDS simulation at 20 torr, and the black line represents the integrated absorbance with no CRDS artifact as derived from our simulations. The top panel shows the lowest concentration data. Above each graph is also shown E_{CRDS} from the simulations are plotted for 20 torr (red) and 630 torr (blue).

Additionally, E_{CRDS} data from the simulations are plotted for both pressures. The experimental and simulated data agree quite well for both pressures over the entire concentration range studied. While $IA(\nu_1)/l_s$ at the two pressures approach each other and the $IA(\nu_1)/l_s$ in the absence of CRDS error at low [HNO_3], the three have not yet converged at the lowest concentrations achieved in this study (8.0×10^{12} molecules×cm^{-3}).

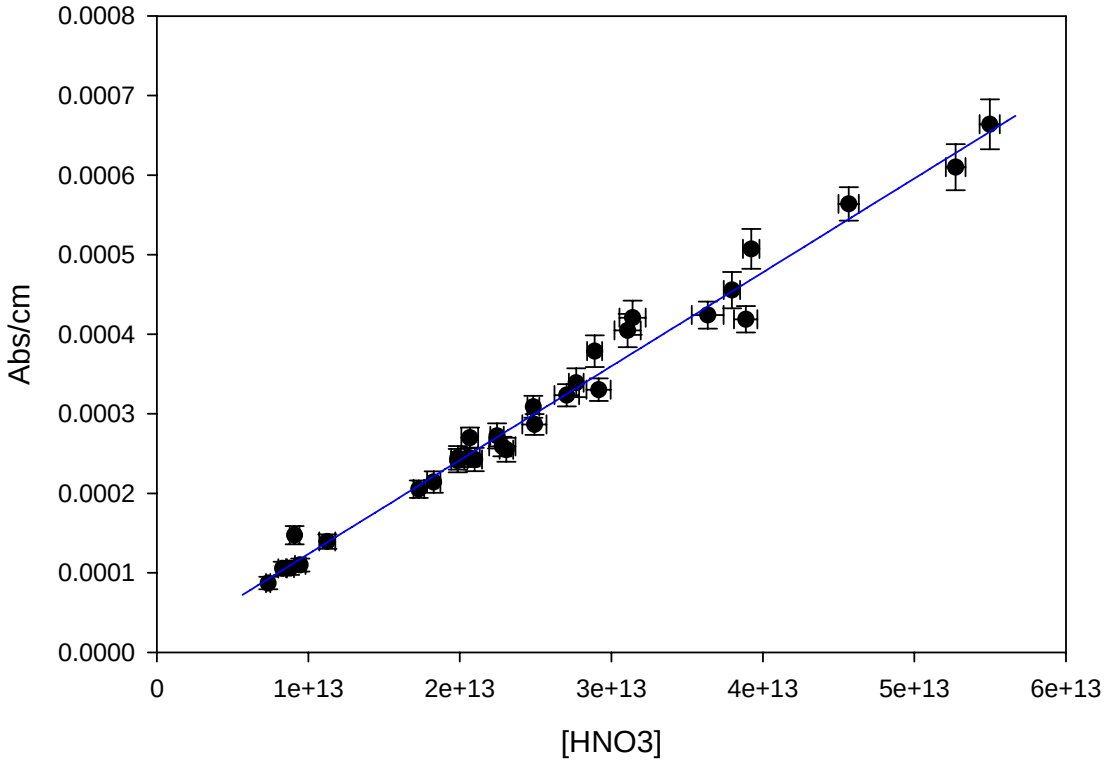

Figure 2.10. Fit to integrated nitric acid ν_1 absorbance data taken at low concentrations (20 and 620 torr). The data is that shown in Figure 2.9 divided by E_{CRDS} to eliminate CRDS fitting errors. The slope of the fit yields a ν_1 integrated cross section of $1.18(08)\times10^{-17}$ cm×molecule^{-1}.

The data used to calculate our measured ν_1 integrated cross section are shown in Figure 2.10. These are the low concentration data shown in Figure 2.9 (both pressures) divided by E_{CRDS} as calculated from the simulations. E_{CRDS} values range from 0.69 to 0.94 for the 20 torr data and from 0.89 to 0.98 for the 630 torr data. The error bars on

each point represent propagated 2σ uncertainties. Uncertainties in the *y*-axis are dominated by the 3% uncertainty in l_s and, for very low-[HNO_3] data, integrated spectral noise, which can contribute up to 5% uncertainty in $IA(\nu_1)$. As described in Section 2.2.3, l_s has been treated as a random error. Uncertainties in [HNO_3] are dominated by the 0.7% uncertainty in I_{185}, which leads to 1%-5% uncertainties in A_{185} and the 6% systematic uncertainty in σ_{185}. Other sources of uncertainty in [HNO_3], uncertainties in the pressure and flow measurements, are less than 1% and therefore contribute little to the overall uncertainty. A weighted fit to the data yields an integrated cross section of $S(\nu_1) = 1.18\pm05(2\sigma)\times10^{-19}$ cm×molecule^{-1}. The *y*-intercept of $5.5\pm10.4\times10^{-6}$ cm^{-1} is within the uncertainty in a single absorbance measurement. We estimate that systematic uncertainties, such as errors in E_{CRDS}, Γ_L, and γ combine to give about 2% additional uncertainty. We therefore report $S(\nu_1) = 1.18\pm08(2\sigma)\times10^{-19}$ cm×molecule^{-1}.

A representative spectrum used to measure $IA(\nu_1)/IA(2\nu_2)$, along with measured and simulated $IA(\nu_1)/IA(2\nu_2)$ data as a function of pressure (at 4×10^{14} molecules×cm^{-3}) are shown in Figure 2.11. The data show an increase in $IA(\nu_1)/IA(2\nu_2)$ with pressure that appears to be converging, but not yet flat, as the pressure approaches 760 torr. The simulated data assume that the $2\nu_2$ band is in the low-signal limit and that the integrated cross section $S(2\nu_2)$ is independent of pressure. Given the excellent agreement between simulations and experiments for the ν_1 band and the poor agreement for $IA(\nu_1)/IA(2\nu_2)$, it appears this assumption is not valid. It is likely that the $2\nu_2$ band, like the ν_1 band, has rovibrational structure that leads to CRDS fitting errors and a pressure dependent apparent cross section. As a result, we have scaled $IA(\nu_1)/IA(2\nu_2)$ assumed in limit of infinite pressure for the simulations to match the data at 760 torr, where the CRDS error

in $2\nu_2$ should be a minimum. There may still be significant CRDS error in $2\nu_2$ at 760 torr, but it is likely smaller than the 15% our simulations predict for the ν_1 band under these conditions. As a result, we add a 10% uncertainty to the 3% uncertainty in our $IA(\nu_1)/IA(2\nu_2)$ at 760 torr to give $S(\nu_1)/S(2\nu_2) = 44\pm5(2\sigma)$, leading to a $2\nu_2$ integrated cross section of $S(2\nu_2) = 2.68\pm.35(2\sigma)\times10^{-19}$ cm×molecule^{-1}.

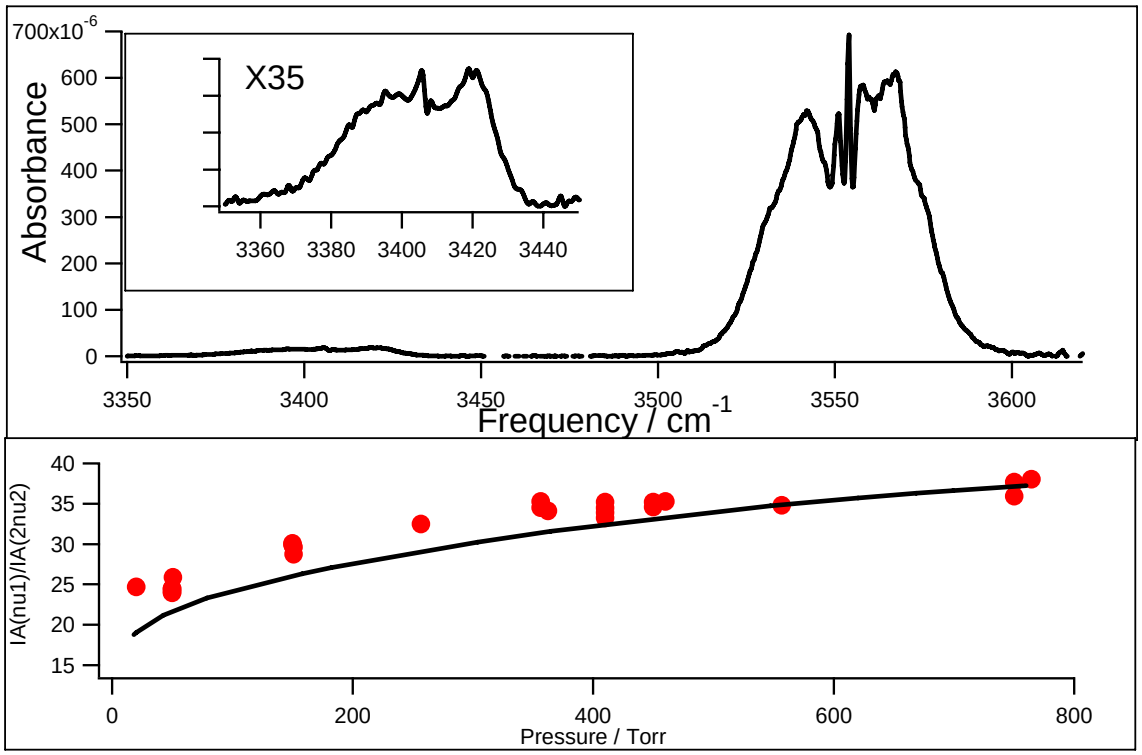

Figure 2.11. Experimentally measured and simulated $S(\nu_1)/S(2\nu_2)$ a function of pressure; data and simulations are both at 4e14 molecules×cm^{-3}. Observed data are shown as diamonds. The line represents simulated data. A representative spectrum used to measure $S(\nu_1)/S(2\nu_2)$ is shown in the top panel.

We have also observed a third nitric acid band at 3220 cm^{-1}. This band was reported previously by Feierabend, Havey and Vaida, but was unassigned [39]. This spectrum of this band along with the $2\nu_2$ is shown in Figure 2.12. The peak at 3220 only has a signal-to-noise ratio of about 8 and has no discernable rovibrational structure. We

measure the ratio of the integrated area of the $2\nu_2$ band to that of this band to be $IA(2\nu_2)/IA(3220) = 7\pm1$, where the uncertainty stems mostly from the uncertainty in the baseline subtraction for the smaller peak. Feierabend et al. report an intensity ratio of 0.029/0.003 = 9.7. If we assume an uncertainty of ±1 in their last reported digits, this ratio is 9.7±3.4. These values agree reasonably well considering the absorbance of this band was near the detection limit in both studies.

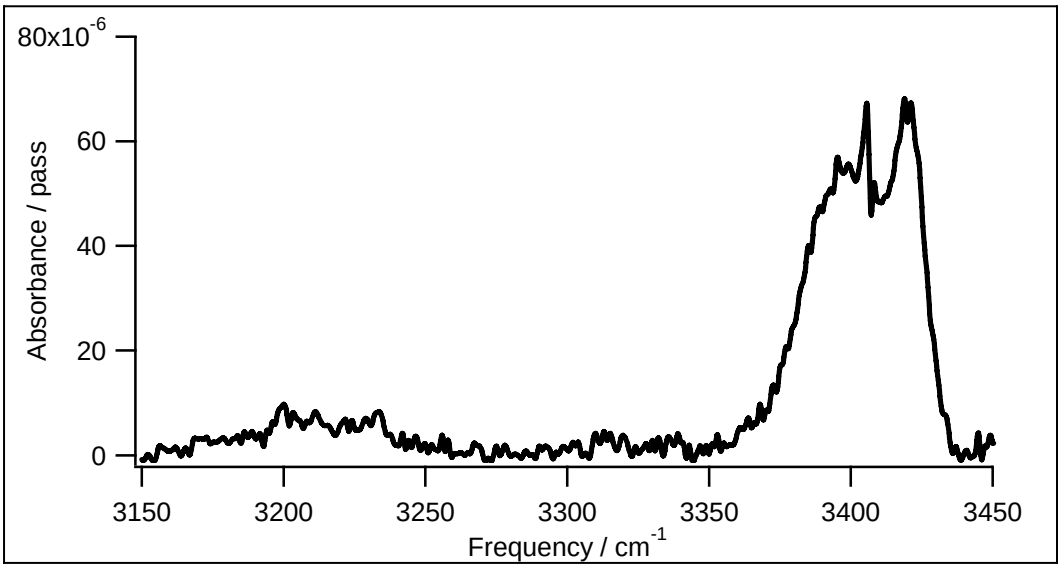

Figure 2.12. Nitric acid $2\nu_2$ band (3400 cm^{-1}) and small unassigned band (3220 cm^{-1}).

While the nitric acid band at 3220 cm^{-1} is quite weak, the high sensitivity of CRDS can magnify the importance of such weak transition. For example, the fitting of HOONO spectra in Chapter 4 was greatly improved once the spectrum shown in Figure 2.12 was used as the nitric acid reference spectrum. Prior to our accounting for the nitric acid peak at 3220 cm^{-1}, we consistently had problems fitting the baseline to the red of HOONO.

2.3.4 Discussion

2.3.4.1 HNO_3 ν_1 Cross Section

The previously reported measurements of $S(\nu_1)$ are listed in Table 2.2. The two previously reported experimental measurements differ significantly despite similarities in methods. Both synthesize nitric acid by addition of nitric acid to a nitrate salt and both use static cells, although Chackerian fills the cell with a small quantity of nitric acid and then charges their cell to 1013 hPa, while Lange does their measurements all at less than 100 torr of pure nitric acid. Both use FTIR, although the resolution for Chackerian, 0.112 cm^{-1}, is much smaller than the 4 cm^{-1} resolution of Lange. The Chackerian study is a detailed study of many different nitric acid bands and carefully measures impurities in the FTIR and subtracts their contributions from the total pressure. If impurities were contributing significantly to the pressure in the Lange study, this might account for their significantly lower value for the cross section. However, the Lange study includes measurements of integrated cross sections for many other molecules as well as overtones and no systematic error appears over their data as a whole.

Table 2.2. HNO_3 ν_1 integrated intensity measured in this work compared to existing literature data.

Study	year	method	integrated intensity / cm molecule^{-1}
this work	2004	flow cell IR-CRDS (1 cm^{-1} resolution)	$1.18\pm0.08\times10^{-17}$
Chackerian et al. [22]	2003	static cell FTIR (0.112 cm^{-1})	$1.238\pm0.024\times10^{-17}$
Lange et al. [23]	2001	static cell FTIR (4 cm^{-1} resolution)	$9.46\pm0.47\times10^{-18}$
Phillips et al. [24]	1998	scaling calculated intensities	$1.40\pm0.20\times10^{-17}$

The procedure used in this experiment of measuring the nitric acid concentration with UV absorption is unique among the measurements of $S(\nu_1)$. Using a continuous and fairly rapid flow has several advantages, primarily a reduced potential influence of nitric acid decomposing or sticking to the walls of the cell. The main drawbacks of this experiment are the uncertainty in the l_s for the IR absorbance and the uncertainty in the correction for CRDS errors. Our measured value of $1.18\pm08(2\sigma)\times10^{-19}$ cm×molecule^{-1} agrees within 5% with the Chackerian et al. value, but deviates significantly from that by Lange et al. and Phillips et al.

2.3.4.2 HNO_3 $2\nu_2$ cross section

There is some discrepancy between the two previous measurements of the nitric acid $2\nu_2$ band. The study by Feierabend et al. does not quote absolute cross sections, but give two values for $S(\nu_1)/S(2\nu_2)$: 38.5 (0.1 cm^{-1} resolution) and 34.5 (1 cm^{-1} resolution). Chackerian et al. report $S(2\nu_2) = 2.82\pm69\times10^{-19}$ cm×molecule^{-1}. This, combined with their value for $S(\nu_1)$ yields $S(\nu_1)/S(2\nu_2) = 44\pm10$. While the Chackerian et al. measurement carefully quantified errors in their nitric acid concentration, their uncertainty in $S(2\nu_2)$ is quite high, presumably due to low signal for this band. The Feierabend et al. paper only measures relative band strengths, so errors in the nitric acid concentration cancel, but the difference between their two measurements is on the same order as the uncertainty in the Chackerian et al. ratio.

Since the focus of this study was the nitric acid ν_1 band, only a narrow range of concentrations were probed in which the $2\nu_2$ band was large enough to measure. As a result, similar to the Fierabend et al. paper, we only directly measure $S(\nu_1)/S(2\nu_2)$ and

then extrapolate $S(2\nu_2)$ from our $S(\nu_1)$ measurement. Because we are measuring the ratio, uncertainties in the nitric acid concentration and l_s cancel. Additionally, our $2\nu_2$ signal is quite large at the concentrations studied. Due to our poor understanding of CRDS errors in the $2\nu_2$ band, our measured $S(\nu_1)/S(2\nu_2)$ and $S(2\nu_2)$ have error bars similar in magnitude to the previous measurements. Our measurement, $S(\nu_1)/S(2\nu_2) = 44\pm5(2\sigma)$, agrees with that of Chackerian et al. and is consistent with the higher value reported by Fierabend et al., but not their lower value.

2.4 Conclusions

The experiments and simulations described in this paper show that using low resolution pulsed ringdown to scan congested spectra can retrieve accurate integrated cross sections, but only under certain conditions. In the limit of high pressure and low concentration, our system yields quantitatively accurate measurements of the nitric acid ν_1 integrated cross section to within 5%. If only one of these conditions is met, measured integrated absorbances can still be reasonably close to the true value. At low concentrations all components of the observed multi-exponential are in the fairly long (microsecond) decay regime and the Zalicki and Zare criterion is met for most of the spectrum. We measure integrated absorbances accurate to better than 20% at 20 torr and $[HNO_3]<1.0\times10^{13}$ molecules$\times$cm^{-3}. At high pressures, pressure broadening causes the molecular spectrum to become homogeneous and the observed ringdowns are well fit by a single exponential. We measure integrated absorbances accurate to better than 20% at 760 torr even at $[HNO_3]>5.0\times10^{15}$ molecules$\times$cm^{-3}.

When neither of these conditions is met, the loss in observed integrated absorbance can be quite dramatic and is strongly concentration and pressure dependent. As shown in Figure 2.9, as concentration increases, the CRDS error increases rapidly and then converges to a constant at high concentrations. We attribute this constant error at high concentrations to a complete loss of contribution from the most intense features in the HNO_3 spectrum to the single exponential fit. At a certain point, while the absorbance due to sharp features contribute decays with such fast lifetimes they are completely missed by the single exponential fits, the rest of the spectrum continues to scale linearly with concentration. The concentration at which the CRDS converges and the magnitude of the error at this concentration both depend on pressure. This convergence of the CRDS error leads to the appearance of linearity in $IA(\nu_1)$ as a function of $[HNO_3]$ if all data is taken in the high-concentration limit. This data can be well fit by a line, but with an offset significantly larger than zero.

When making quantitative measurements of congested spectra using low-resolution CRDS, care must be taken to ensure this is not the operating regime. As shown in this study, if a high-resolution spectrum of the feature being investigated is available, it is possible to correct rovibrational spectra taken by low-resolution CRDS and derive accurate absorbances to within 5% through the use of CRDS simulations. However, if a high-resolution spectrum is not available, quantitative measurements should be accompanied by demonstrations that the experiment is being carried out in a regime where such measurements are accurate. We suggest two such demonstrations: (1) Show that the absorbance as measured by CRDS is not only linear with concentration,

but has an intercept very close to zero. (2) Show that the apparent integrated intensity for the band is independent of pressure over a wide range.

The $HOONO/HONO_2$ branching ratio measurements we published in Bean et al. [7] (Chapter 3) recognized that CRDS errors may have impacted measurements of $HONO_2$ absorbances, but had a poor understanding of the magnitude of these errors. We previously assumed $E_{CRDS} = 0.9$, but now estimate for those conditions that E_{CRDS} should be 0.4. This dramatically reduces the reported branching ratio by more than a factor of two. The later CRDS measurements of the $HOONO/HONO_2$ branching ratio (chapter 3) have used the results of this chapter to correct integrated absorbances as a function of concentration and pressure to derive accurate $HOONO/HONO_2$ branching ratios.